IMAGING METHODOLOGY – Full Papers

Magnetic Resonance in Medicine 79:2511–2523 (2018)

Hybrid Ultrasound-MR Guided HIFU Treatment Method With 3D Motion Compensation

Zarko Celicanin,[1,2]* Gibran Manasseh,[3] Lorena Petrusca,[4] Klaus Scheffler,[5,6] Vincent Auboiroux,[3,7] Lindsey A. Crowe,[8] Jean-Noel Hyacinthe,[3,9] Yutaka Natsuaki,[10] Francesco Santini,[1,2] Christoph D. Becker,[4,8] Sylvain Terraz,[3,8] Oliver Bieri,[1,2] and Rares Salomir[3,8]

Purpose: Treatments using high-intensity focused ultrasound (HIFU) in the abdominal region remain challenging as a result of respiratory organ motion. A novel method is described here to achieve 3D motion-compensated ultrasound (US) MR-guided HIFU therapy using simultaneous ultrasound and MRI.

Methods: A truly hybrid US-MR-guided HIFU method was used to plan and control the treatment. Two-dimensional ultrasound was used in real time to enable tracking of the motion in the coronal plane, whereas an MR pencil-beam navigator was used to detect anterior–posterior motion. Prospective motion compensation of proton resonance frequency shift (PRFS) thermometry and HIFU electronic beam steering were achieved.

Results: The 3D prospective motion-corrected PRFS temperature maps showed reduced intrascan ghosting artifacts, a high signal-to-noise ratio, and low geometric distortion. The k-space data yielded a consistent temperature-dependent PRFS effect, matching the gold standard thermometry within approximately 1°C. The maximum in-plane temperature elevation ex vivo was improved by a factor of 2. Baseline thermometry acquired in volunteers indicated reduction of residual motion, together with an accuracy/precision of near-harmonic referenceless PRFS thermometry on the order of 0.5/1.0°C.

Conclusions: Hybrid US-MR-guided HIFU ablation with 3D motion compensation was demonstrated ex vivo together with a stable referenceless PRFS thermometry baseline in healthy volunteer liver acquisitions. **Magn Reson Med 79:2511–2523, 2018. © 2017 International Society for Magnetic Resonance in Medicine.**

Key words: hybrid imaging US/MR; real-time motion compensation; focused ultrasound ablation; PRFS thermometry

INTRODUCTION

High-intensity focused ultrasound (HIFU) is the concept of using acoustic energy to induce thermal coagulation inside the human body (1). Although initially developed in the 1940s, the technique was significantly advanced in the 1990s with the introduction of accurate thermal ablation monitoring by MRI. Magnetic resonance imaging and ultrasound (US) imaging were established as the preferred guiding modalities (2–4), as they are innocuous in a clinical setting, while having complementary guiding characteristics. Combining MRI and HIFU into MR-guided high-intensity focused ultrasound (MRgHIFU) has given rise to clinically approved therapies (2–5).

Magnetic resonance imaging offers excellent soft-tissue delineation necessary for treatment planning and evaluation of the treatment outcome. Conversely, US imaging generally offers poor conspicuity between soft tissues, limiting its guiding capabilities. Furthermore, MRI is the only clinically proven imaging modality capable of monitoring thermotherapies by providing thermal quantitative maps required for thermal dose calculation (6). However, considering that a US system is by far the most affordable imaging modality, and taking into account its high temporal and spatial resolution (submillimeter current state-of-the-art) as well as its insensitivity to geometrical distortions, US imaging is also a suitable candidate for guiding HIFU (7).

Considering the complementary strengths and weaknesses of the imaging capabilities of both MRI and US, the two techniques could be combined to form a hybrid US-MRI guiding method. Magnetic resonance imaging–compatible US imaging transducers have already been developed, tested, and reported (8–10).

Abdominal organ motion, caused by respiration and other physiological processes, renders the already developed clinical methods for local therapy in immobile organs (e.g., the prostate (11) or uterus (fibroids) (12))

[1]Department of Radiology, Division of Radiological Physics, University of Basel Hospital, Basel, Switzerland.

[2]Department of Biomedical Engineering, University of Basel, Basel, Switzerland.

[3]Image Guided Interventions Laboratory, Faculty of Medicine, University of Geneva, Geneva, Switzerland.

[4]Hepatobiliary and Pancreatic Interventional Radiology, Faculty of Medicine, University of Geneva, Geneva, Switzerland.

[5]MRC Department, MPI for Biological Cybernetics, Tübingen, Germany.

[6]Department of Biomedical Magnetic Resonance, University of Tübingen, Tübingen, Germany.

[7]Clinatec/LETI/CEA, 38054, Grenoble, France.

[8]Radiology Department, University Hospitals of Geneva, Geneva, Switzerland.

[9]School of Health Sciences, HES-SO, University of Applied Sciences and Arts of Western Switzerland, Geneva, Switzerland.

[10]Siemens Medical Solutions Inc, Los Angeles, California, USA.

*Correspondence to: Zarko Celicanin, Ph.D., Division of Radiological Physics, Department of Radiology, University of Basel Hospital, Petersgraben 4, 4031 Basel, Switzerland. E-mail: zarko.celicanin@unibas.ch

The authors would like to thank the Swiss National Science Foundation for the financial support of this work (grants CR33I3_143980 and 326030_150816). Dr. Yutaka Natsuaki was employed by Siemens Medical Solutions at the time of the reported study.

Received 24 January 2017; revised 10 August 2017; accepted 11 August 2017

DOI 10.1002/mrm.26897

Published online 24 September 2017 in Wiley Online Library (wileyonlinelibrary.com).

inapplicable in the abdominal region. Previous attempts to handle respiratory motion of organs guided solely by MRI include the following: organ motion compensation using principle component analysis, used in a pretreatment step to record the organ motion pattern (13); estimation of the motion pattern during an initial learning phase, with monitoring of the target motion by image registration (in-plane motion) and a pencil-beam navigator (out-of-plane motion) during treatment (14); an external respiratory bellow used in a treatment phase to provide target motion estimation from a premapped signal acquired in an initial preparative training (15); and HIFU beam steering and simultaneous prospective motion compensation of MR thermometry using an MR pencil-beam navigator (16). In (6,17,18), ex vivo feasibility studies demonstrated the ability of ultrasound to guide HIFU therapy simultaneously to MR thermometry, enabling the focal point to follow the organ motion in two dimensions. This study excluded out-of-plane motion compensation as a result of the unavailability of a 3D MR-compatible US transducer. Furthermore, no explicit intrascan motion correction was applied to the MR data, but simply a rapid acquisition (300 ms/slice) was performed to alleviate intrascan ghosting artifacts. Respiratory-gated MRgHIFU in the upper abdomen, using an MR-compatible in-bore digital camera, was recently reported (19). Contrary to US image–based monitoring of abdominal motion, the use of an optical camera does not require an additional acoustic window; however, only the surface of the body can be analyzed with no direct visualization of the target tissue motion.

Temperature imaging based on the proton resonance frequency shift (PRFS) is the favored method to measure the temperature distribution, as it is tissue independent, linear, and provides a high signal-to-noise ratio (SNR) (20). The application of PRFS-based temperature mapping in the abdominal region requires organ motion compensation. Various approaches have been suggested to deal with the motion, of which the baseline and multibaseline were the most common. Referenceless thermometry was suggested by Rieke et al ((21)) and can be used for nonperiodic motion (21). The referenceless temperature calculation method has been demonstrated to be a robust and simple solution for noninvasive ablation in the abdominal region, whereas the multibaseline approach is more accurate for interventions in areas with strong B_0 inhomogeneities (22,23). An improvement of the referenceless thermometry, which enables an estimation of the background phase in the presence of phase discontinuities between aqueous and adipose tissues, was described in (24).

We demonstrate here a truly hybrid US-MR-guided HIFU (US-MRgHIFU) method using an ex vivo study of thermoablation with electronic steering of the acoustic beam in three dimensions, and prospective motion compensation of multislice MR thermometry. In addition, baseline volunteer data in the liver were analyzed. Ultrasound images acquired in the coronal orientation were complemented by an MR-based pencil-beam navigator (25,26), oriented perpendicular to the US imaging plane to achieve full 3D organ motion compensation. The 3D target motion vectors were sent in real time to the HIFU system, allowing its focal point to be repositioned. The same information was simultaneously used for prospective motion compensation of the MR thermometry, which was acquired using a segmented gradient-recalled echo (GRE) echo-planar imaging (EPI) pulse sequence.

METHODS

Instruments

All measurements were performed using a 3T whole-body MR system (MAGNETOM Trio, Siemens AG, Erlangen, Germany). For ex vivo experiments, a receive-only loop coil of 11-cm diameter was used, whereas multi-element surface coils were used in volunteers (typically nine elements of the spine coil plus nine elements of the body coil).

The spherical HIFU transducer (Imasonic, Besançon, France) consisted of 256 phased-array elements (frequency range $f = 974–1049$ kHz, focal length $R = 130$ mm, aperture $D = 140$ mm). It delivered 300 W of maximum acoustic power and was supplied with a 256-channel beam former (Image Guided Therapy, Pessac, France). Further details on hardware are provided in previous reports (17,22).

The acquisition of US images was performed using a clinical US system (ACUSON Antares, Siemens Healthcare, Mountain View, CA). The abdominal CH4.1 imaging probe (256-element phased-array transducer) was modified to ensure MR compatibility by replacing various magnetic materials with MR-compatible ones. Further technical details of the MR-compatible US imaging device can be found in (27).

Ex Vivo Ablation Protocol

Ex vivo bovine liver was used for the experiments and was placed in an ultrasound transparent bag, then immersed in a water-filled container, acoustically coupled with the water tank hosting the HIFU transducer. A mechanical ventilator was used to produce a breathing-like motion pattern by pumping air in and out of a balloon, which acted as a simulated lung. A wooden arch was used to provide the support for a rotation axis, such that the suspended sample underwent periodic oscillations driven by the inflating balloon, as illustrated by Auboiroux et al (17). The US probe was positioned to acquire images of the moving sample in an approximate coronal (horizontal) plane. The US imaging plane was set approximately 10 to 15 mm above the HIFU focal point. Periodic motion was obtained by the gravitational force recalling the sample toward its equilibrium position during the gradual deflation of the balloon. The prospective motion compensation was in the horizontal plane (i.e., the coronal orientation) in the MR coordinate frame. The available motion amplitude of the simulated breathing-like motion was in the range of 6 to 15 mm, and was controlled by the volume of the air pumped by the ventilator. The period of the motion was in the range of 6 to 10 s, similar to the typical breathing pattern of a human subject. Several HIFU sonications of 36-s duration and an average acoustic power of 150 W were performed with and without motion compensation. Attenuation of

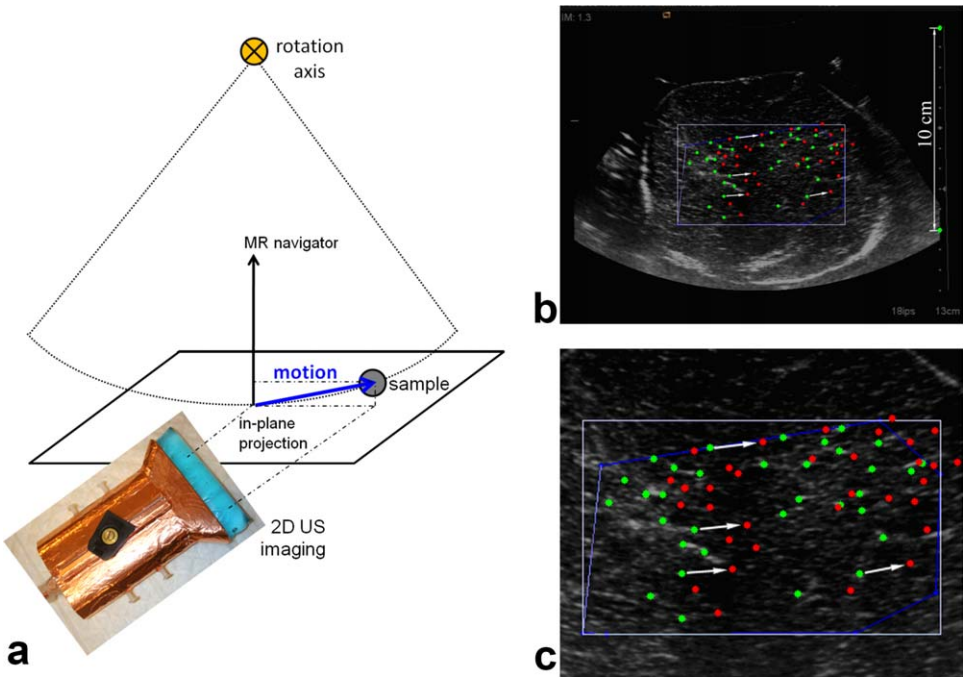

FIG. 1. Setup of the US and MR imaging systems for the guidance of HIFU sonication in moving tissue. **a**: The sample undergoes a circular motion, with the principal component in the US imaging plane (horizontal) and the vertical displacement being detected by the MR navigator. **b**: Ultrasound imaging–based motion tracking in the horizontal plane; second harmonic data from the ex vivo tissue are shown (Fo = 2.2 MHz, mechanical index = 1.3, frame rate = 18 fps). The registration points for feature tracking are overlaid. Two extreme situations are shown, corresponding to high volume (red dots) and low volume (green dots) of air in the inflating balloon (i.e., comparable to exhalation and inspiration). Selected 2D motion vectors are indicated with white arrows. Note the distance scale on the right side. **c**: The ROI of frame (**b**), zoomed-in by a factor of 2.

focal point intensity during lateral beam steering was compensated for using a precalibrated lookup table.

To examine the effectiveness of the motion-compensated treatment, three series of experiments were performed: (i) static HIFU focal point position (i.e., no motion compensation); (ii) 2D motion compensation of the instantaneous position of the HIFU focal point, aiming to cancel the motion components in the US imaging plane; and (iii) 3D motion compensation of the HIFU ablation using the combined information of US imaging and MR navigator. Magnetic resonance thermometry was 3D motion-compensated in each case to enable accurate monitoring of the resulting thermal build-up. The anisotropy and shape of the thermal build-up and gross pathology, as performed immediately after the experiment, were used to assess the quality of the motion-compensated ablation. Similar to (16), calibration experiments were performed in static tissue (ventilator off) using the same setup to guarantee that there was no intrinsic acoustical aberration of the HIFU beam.

Imaging and Real-Time Data Processing

The horizontal projection of the motion vector of the tissue (Fig. 1a) was imaged by second harmonic ultrasonography and tracked via the acoustic speckle shift, typically in the coronal plane (horizontal). The US field depth was approximately 10 to 18 cm with single-focus scanning. The frame rate varied between 15 and 30 images per second, depending on the field depth and angular aperture. The slice thickness of the US imaging plane was approximately 4 mm (carrier frequency = 2.2 MHz, receive central frequency = 4.4 MHz). Further US imaging parameters are provided in (27).

The US images were sent at a frame rate of 30 Hz in near real time to an external PC, which extracted the average motion vector in-plane over a user-defined region of interest (ROI) (see Figs. 1b and 1c). As opposed to the real-time feedback in MR navigator, near real-time feedback here refers to grabbing the images from the US imaging unit, processing the images to extract the motion fields, and transferring the data, which takes approximately 30 ms. The PC further controlled the HIFU system and communicated the respective 2D motion vector to the MR system on the fly.

To control the exact horizontal orientation of the US probe in the MR coordinate system (and therefore the US imaging plane), volume imaging with a T_1-weighted 3D GRE pulse sequence was performed (echo time = 2.99 ms, repetition time (TR) = 6.88 ms, flip angle = 10°, voxel size = $1.2 \times 1.2 \times 2\,mm^3$). The assessment of the US probe orientation was based on the known shape of the transducer's holder and the spatially smooth MR signal of the acoustic coupling gel, used to fill the gap between transducer, holder, and sample. Once the US image was imported into the external PC, an optical flow algorithm was used to calculate the average displacement vector within a user-defined ROI. This was achieved using an

in-house program based on OpenCV libraries (Open Source Computer Vision Library, http://www.opencv.org/) running on a standard personal computer (Intel Core Duo P8700 CPU, 2.53GHz, 2 GB RAM). Registration points were automatically assigned to sharp edge features inside the user-defined ROI using a feature-detection algorithm (see Figs. 1b and 1c). This used the OpenCV "GoodFeaturesToTrack" method, which was implemented based on the algorithm described in (28). Once the landmarks were initialized, the displacement could be tracked by computing the optical flow using the iterative Lucas-Kanade method (29) and pyramidal implementation (30). The 2D motion vectors were calculated iteratively between two consecutive frames. This algorithm does not produce cumulative errors if the landmarks are detected correctly in each image frame. However, one corrupted frame (e.g., HIFU signal interferences) may yield permanent errors in the subsequent frame tracking, requiring a redefinition of the reference frame. They were projected on two orthogonal axes and averaged over the set of landmarks, yielding rigid correction for the translation motion and losing the information on eventual local rotation.

Aiming for measurement of the motion vector in 3D, a pencil-beam MR navigator was used concurrently to track the remaining anterior–posterior (AP) (vertical) direction. The MR navigator consisted of a 2D spatially selective echo-planar radiofrequency pulse, used to excite a strip-shaped column, followed by a GRE readout. The acquisition duration of the pencil-beam navigator was approximately 20 ms, while the navigator volume was a rectangular column of dimension (5 to 10) × (5 to 10) × 180 mm, capturing the information from the tissue–air interface. Further details are provided in (16).

The acquired MR images were reconstructed and exported in real time via an Ethernet connection to the external PC. A software package, Thermoguide (Image Guided Therapy, Pessac, France), was used for the calculation of thermal maps based on a 2D near-harmonic referenceless PRFS method (22), which was implemented using the closed border variant in the coronal plane (perpendicular to the HIFU beam) and using the open border variant in the sagittal plane (parallel to the beam), to avoid contamination of the border phase from ultrasound heating. Typically, 30% of the circular perimeter was open, symmetrically, both proximal and distal to the HIFU transducer.

Acoustic energy emitted by the HIFU transducer may interfere with US imaging, yielding fringe artifacts in the ultrasound image. As the SNR of back-scattered ultrasound images was decreasing with distance, typically these artifacts initially occurred in the image region corresponding to the far field (17). These transient artifacts can hinder the motion-tracking algorithm, introducing bias to the estimated trajectory. To maintain a sufficient level of robustness without compromising on the US imaging gain, and thus sensitivity, a rejection filter was implemented. The acoustic interference artifacts occurred suddenly and without spatial coherence, rendering some landmarks temporarily unavailable. The incremental displacement of a given landmark (k) between successive frames ($n-1$, n) is denoted as $\Delta\vec{r}_k(t_n, t_{n-1})$. Given the experimental conditions, it is supposed that the tracked landmarks in the US image undergo a continuous and smooth trajectory; therefore, a threshold value (δ) was defined for the allowed magnitude of the incremental displacement of landmarks. If the actual incremental displacement of a landmark was detected to be shifted by more than the specified threshold (δ), set here to 2 mm (equivalent to 60 mm/s maximum velocity at 30 fps imaging rate), this was considered an artifact produced by HIFU signal interference. The current position of that landmark was not measured in the actual US image, but instead was substituted by an estimated average position of the noncorrupted landmarks in the same image (see equation below). The number of noncorrupted landmarks in the US imaging frame (n) is denoted as N.

$$\vec{r}_k(t_n) = \vec{r}_k(t_{n-1}) + \frac{1}{N}\sum_{||\Delta\vec{r}_j(t_n,t_{n-1})||<\delta}^{N} \Delta\vec{r}_j(t_n, t_{n-1})$$

This approach is equivalent to adaptive temporal undersampling of regions in the US images.

The interrelation scheme between the different parts of the complete system with the estimated delay times is shown in Figure 2. Note that single-line arrows correspond to one-dimensional information, double line to 2D, and triple line to 3D. The 2D vector extracted from the US data (motion along Ox and Oz axes of the MR magnet) was then sent to the MR system via an Ethernet connection. The image reconstruction unit combined the out-of-plane motion measured by the MR pencil-beam navigator with the US tracking to form a complete 3D motion vector, which was then sent back via Ethernet to the HIFU beam-former driving application. The updated frequency of the HIFU focal spot steering was equal to one per TR of the MR thermometry pulse sequence (i.e., approximately 15 Hz). The HIFU emission was practically continuous during a dynamic steering, but an additional latency of up to 20 ms existed between the moment of Ethernet communication to the multichannel generator and the effective update of the acoustic beam. Acquiring and importing 2D US data and online calculation of motion vectors was more time-consuming than acquiring and processing one-dimensional MR pencil-beam navigator data. Therefore, the latency from US acquisition to HIFU beam update (approximately 75 ms) was longer than the latency from MR navigator acquisition to HIFU beam update (approximately 45 ms).

MR thermometry was performed based on the PRFS effect using a segmented GRE-EPI sequence. The imaging parameters were as follows: echo time = 10.5 ms, TR = 68 ms, flip angle = 15°, acquisition matrix = 128 × 121, reconstructed matrix = 256 × 256, slice thickness = 5–8 mm, bandwidth = 797 Hz/px, EPI factor = 11, field of view = 192 × 192 mm^2 (ex vivo) or 256 × 256 mm^2 (human volunteer), acquisition duration per slice = 0.75 s, phase-encoding direction = head–foot (HF). Note that the TR parameter of the GRE-EPI thermometry sequence also includes the duration of the MR navigator. Fat suppression was implemented using a water-selective 1-2-1 binomial radiofrequency pulse for slice excitation. To correct

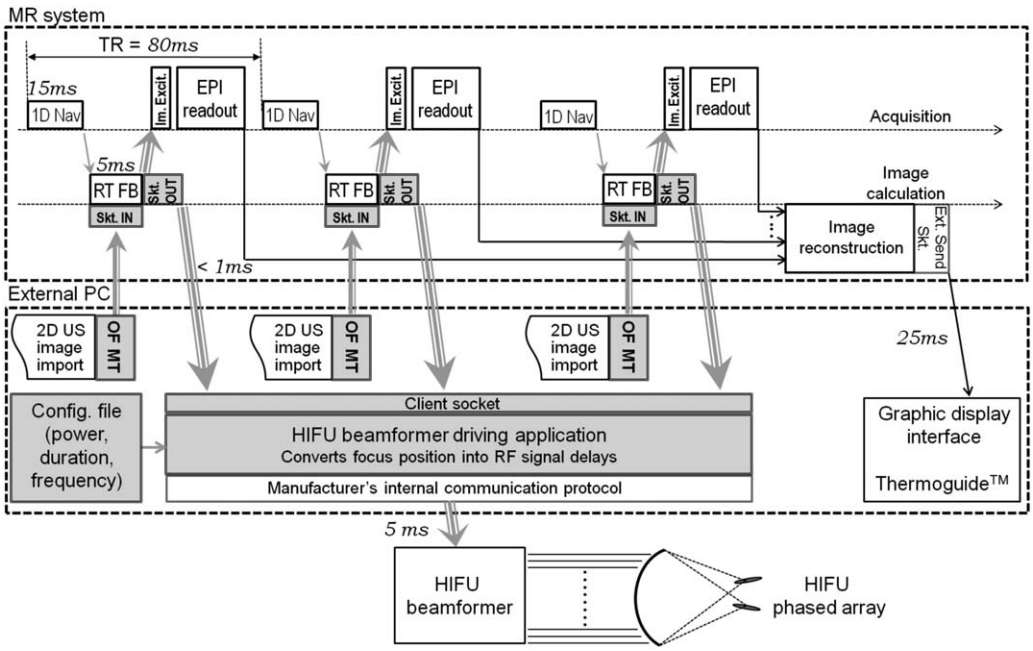

FIG. 2. Diagram of the system showing the relationship and information exchange among the MR system, external PC, and HIFU system. The dimensionality of the motion information is indicated by the line style of the arrows (single, double, or triple for one-dimensional projection, 2D projection, or full 3D vector, respectively), and the latencies of the essential processes are provided.

for tissue motion, while also increasing the SNR and reducing the geometrical distortion, the imaging plane was repositioned for each new segment of k-space. This was achieved by adapting the phases of the digital receivers sampling the MR signal, according to the Fourier shift theorem, and the central frequency of radio-frequency pulses, on a segment-per-segment basis, for the actual field of view shift at the time acquisition of each echo train. To have multiple-axis control of the sonication, the MR thermometry was performed in two perpendicular planes: the first in a coronal orientation (i.e., parallel to the HIFU transducer, if present), and the second in a sagittal orientation. The slices were acquired sequentially (i.e., the complete k-space of each plane was acquired before beginning the acquisition of the second plane). The duration to acquire one slice (0.75 s) resulted in an overall temporal resolution of 1.5 s. It is important to note that the temporal resolution of the motion compensation was the TR of radiofrequency slice excitation (here, 68 ms, equivalent to 14.7 Hz) and not the temporal resolution of the MR thermometry imaging.

Consistency of Segmented GRE-EPI Phase Information During the Continuous Reprogramming of the Slice Selection

Reprogramming the acquisition of the k-space segments of a moving object followed by full-slice MR reconstruction may yield inconsistencies as a result of switching conditions. Therefore, the consistency of segmented GRE-EPI phase information and the accuracy of PRFS-derived thermometry during motion-compensated MR acquisition were evaluated using a "gold standard" fluoroptic temperature sensor with a tip diameter of 0.8 mm (STF Fast Response Immersion Probe, Luxtron, Santa Clara, CA). The sensors were calibrated before the MR experiment, and the manufacturer guaranteed the accuracy of $\pm 0.5^{\circ}C$ in the temperature range of 0 to $295^{\circ}C$, with a response time of 250 ms in water. The temperature was recorded every second at the tip of the optical probes using a fluoroptic thermometry system (FOT Lab-Kit, Luxtron, Santa Clara, CA) and its associated software for interface with a PC.

A specific setup was designed and implemented r to avoid direct absorption of HIFU energy by the fluoroptic fiber tip, which would bias the comparison between the true tissue temperature as seen by PRFS thermometry and that seen by the fiber tip measured by the laser fluorometer. For this purpose, the optical fiber was positioned inside a 14-G catheter sheath, taking advantage of the thinner diameter of the 20-mm length tip as compared with the optical fiber body (see Figs. 3a–3d). This configuration created a uniform air layer of approximately 0.5 mm between the sensor and the surrounding sheath, acting as a strong impedance barrier for the propagation of HIFU between tissue and sensor. Typically, the acoustic impedance ratio between air and tissue is 3000, corresponding to a total wave reflection at the interface. Importantly, the thickness of this air barrier was superior to the acoustic wavelength in air (0.34 mm at 1 MHz); therefore, theoretically, negligible evanescent waves reached the sensor.

The embedded sensor was easily visible on MR images in both the T_1-weighted 3D GRE for planning (Figs. 3e and 3f) and the PRFS GRE-EPI for temperature monitoring. It served as a spatial target for the HIFU sonication. As explained in (16), although the motion was tracked and k-space segments were re-aligned to freeze the motion, the displacement of the tissue sample modified the local magnetic field, thus requiring multibaseline or

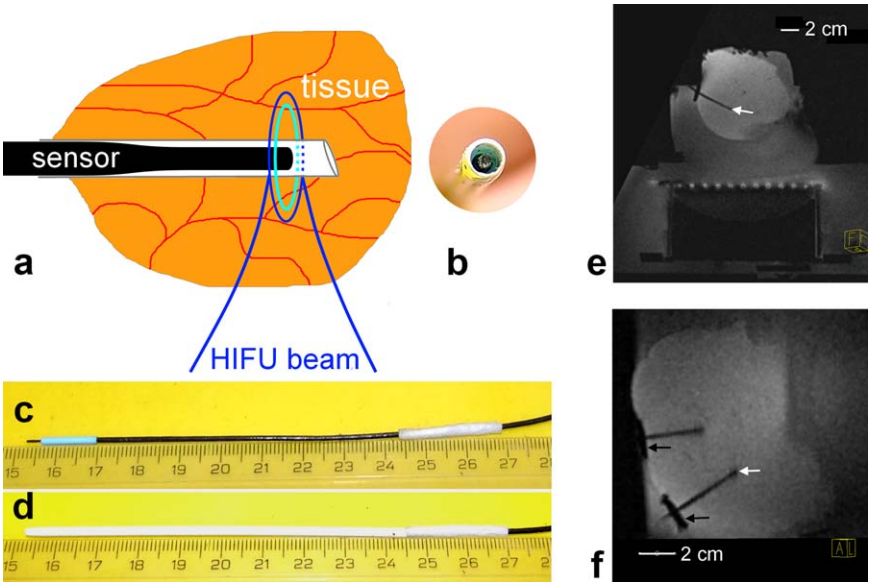

FIG. 3. Design of an acoustically shielded temperature sensor and its positioning under MR guidance. **a**: Schematic drawing of the sensor and shielding sheath. **b**: High-resolution top-view photography demonstrating the concentric structure of the device. **c, d**: Photography of the optical fiber body and coaxial sheath. **e, f**: T_1-weighted images of the setup in transverse and coronal plane, respectively. The focal spot of the HIFU transducer was positioned at the tip of the sensor.

referenceless MR thermometry. The disruption of the local susceptibility by the embedded sensor did not permit, in this case, a straightforward use of referenceless MR thermometry. The temperature data read by the sensor were compared with the PRFS phase shift in the pixels adjacent to the sensor tip, using a multibaseline time-referenced subtraction (31). Motion-compensated segmented GRE-EPI acquisition, and fixed focal point (i.e., tissue "self-scanning" through the HIFU beam) or motion-tracked focus sonication were performed in moving samples. In motion-tracked mode, the HIFU focal point followed the position of the optical sensor tip.

Volunteer Study

Four healthy volunteers (34-year-old male, 40-year-old male, 25-year-old female, and 29-year-old male) were scanned, after signing an informed consent and following the guidelines of the local internal review board. The MR-compatible US imaging was performed intercostal in the coronal plane, similar to (27) but the shielded holder of the US imaging transducer was immobilized horizontal in this study using sand bags during the acquisition. Careful alignment of the US imaging symmetry axis was performed along the left–right (LR) direction using the integrated laser guide of the MR scanner. Acoustic coupling to the skin was achieved using standard ultrasonic gel (Aquasonic 100, Parker Laboratories, Fairfield, NJ). A pencil-beam navigator monitored the AP breathing motion of the upper abdominal wall. Real-time navigated PRFS thermometry was performed as described previously. Radiofrequency saturation slabs were added as needed to avoid artifacts from foldover or heart motion. The visibility of blood vessels, exploiting the inflow T_1-weighted hypersignal, was verified and the flip angle adjusted accordingly. The blood-vessel locations were tracked in the postprocessing of motion-compensated segmented GRE-EPI magnitude data to assess the residual in-plane motion. The blood vessel was seeded manually in each frame, then segmentation was applied to extract the hyperintense voxels belonging to that blood vessel. Finally, the coordinates of the "center of mass" of the hyperintense voxels were computed on a frame-by-frame basis.

The tracking factors along the HF, AP, and LR directions, in this order, were optimized by interactively changing their values by a step of 0.05, while an expert user compared the apparent residual motion of blood vessels to reference static targets on the screen. The actual tracking values depended on the orientation of the US imaging plane and the respective MR pencil-beam navigator, as well as on the local deformations of the tissue.

The motion-compensated GRE-EPI phase consistency was investigated in healthy volunteer liver data by applying the near-harmonic referenceless method (22) for a circular ROI of 52-mm inner diameter positioned on the liver dome in the coronal slice, allowing at least a 5-pixel (around 1 cm) free margin from the diaphragm. The temporal stability of the referenceless PRFS thermometry was investigated by calculating the pixel-wise standard deviation of the baseline over 2 min of continuous acquisition.

RESULTS

Ex Vivo Motion-Compensated PRFS Thermometry and HIFU Sonication

Simultaneous imaging with US and MRI was without mutual interference. The US images were of standard quality, enabling the tracking algorithm to be both stable and accurate. The HIFU sonication produced detectable acoustic interference in the far field of the US images. Interferences increased with the applied HIFU power level and could be attenuated by appropriate adjustment of the US scanner–transmitted power and receiver gain. On-the-fly stabilization of landmark tracking using the adaptive filter was sufficient in all explored cases of this study to enable continuous calculation of the average motion vector in the region of interest. The accuracy of

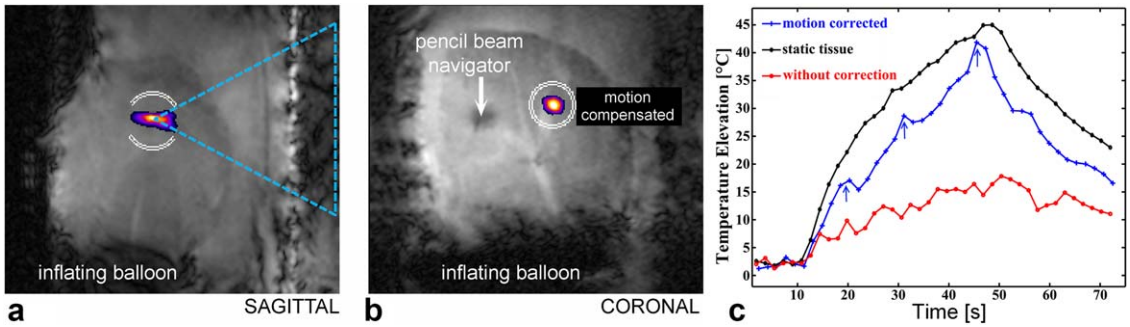

FIG. 4. **a, b**: Magnitude data and referenceless thermometry shown in two orthogonal planes, demonstrating the geometry of the HIFU beam ex vivo and the trace of the MR pencil-beam navigator. **c**: Temperature elevation versus time as measured by referenceless PRFS for three representative conditions of sonication (150 W, 36 s): static tissue, motion-corrected with moving tissue and no correction in moving tissue. Applied acoustic power was compensated for lateral steering when motion tracking was used. Vertical arrows indicate the residual perturbation from breathing cycles.

the landmark tracking process was found to be approximately 85 μ.

An example of motion-compensated sagittal and coronal PRFS temperature maps of standard quality, based on the segmented GRE-EPI navigated sequence, is shown on Figures 4a and 4b, demonstrating the geometry of the HIFU beam and the position of the MR pencil-beam navigator (note the dark saturation-induced region, indicated by a white arrow). The highest temperature elevation in the sonicated area versus time is plotted in Figure 4c for three representative conditions using the same HIFU parameters: (i) static tissue, (ii) moving tissue with no compensation, and (iii) moving tissue with real-time steering for compensation. Considering the static sonication as reference, the motion-compensated sonication yielded a very similar temperature elevation still less effective. Together with the visible peaks being synchronized to the breathing cycle, this is indicative of the remaining minor imperfections of the coordinate matching between the tissue and the focal point.

Figure 5 shows the results of three independent HIFU sonication experiments achieved without motion compensation in one tissue sample (ex vivo bovine liver). The elevated temperature at the sonication end point (36 s) is shown in two orientations, sagittal and coronal, and the corresponding thermal dose in coronal orientation is calculated according to (6) and shown in the last column. Because of the motion of the ex vivo liver, the acoustic energy is dispersed around the desired focal point, resulting in lower temperature elevation, elongated thermal build-up, and therefore less-effective ablation. Note that the temperature distribution generated by noncompensated sonication represents the spatio-temporal convolution between the motion trajectory of the tissue and a Gaussian kernel, which is the temperature profile yielded by a very short HIFU sonication in static tissue. Gross pathology on fresh tissue did not show decolored areas, as the absolute elevated temperature was probably below the coagulation threshold.

Figure 6 shows the ablation achieved by the hybrid US-MRgHIFU with 3D motion compensation in three independent experiments on another sample of tissue taken from the same organ as in Figure 5. Sagittal and coronal views of the elevated temperature at the sonication end point (after 36 s) are presented. From the gross pathology, performed after the experiment, the ablated tissue (decolored area) is primarily isotropic. The elevated temperatures, greater than 30 °C, were high enough to cause the coagulation of the liver tissue. It should be noted, however, that fresh tissue cutting cannot guarantee a perfect alignment with the MR coronal plane used in the treatment setup. In some cases, the MR thermometry sagittal slice was slightly misaligned from the focal point trajectory (e.g., sagittal map in the third raw data); in these cases, the temperatures measured are not representative of the highest thermal build-up actually produced in the tissue. The coronal plane always captured the focal spot because of its elongated shape.

When comparing quantitatively the experiments shown in Figures 5 and 6, the maximum temperature elevation achieved at the end of a 36-s sonication in a tissue sample, originating from the same animal liver, was on average 41.2°C with motion compensation, and 20.0°C without motion compensation. This corresponds to an average improvement of maximum-induced temperature by a factor of approximately 2. When scaled to the static tissue sonication according to Table 1, the maximum temperature elevation ratio was on average 45% without motion tracking, 81% using only the 2D compensation of the principal components captured here by the US imaging plane, and 94% with 3D motion tracking.

Phase Stability of GRE-MR Signal During Motion Tracking Acquisition

Preliminary experiments (data not included) carried out under static conditions and moderate heating (i.e., not triggering tissue boiling or cavitation at the focus), using fixed-focus HIFU sonication with the focal point positioned approximately on the fluoroptic sensor, demonstrated that the temperature elevation measured by the time-referenced or referenceless PRFS method and the acoustically shielded fluoroptic sensor agreed within a deviation of 1°C.

Figure 7 illustrates the comparison between the same fluoroptic sensor data and motion-compensated multibaseline PRFS thermometry in the proximity of the sensor for the condition of moving tissue, with and without HIFU focal point tracking of tissue motion. The applied acoustic

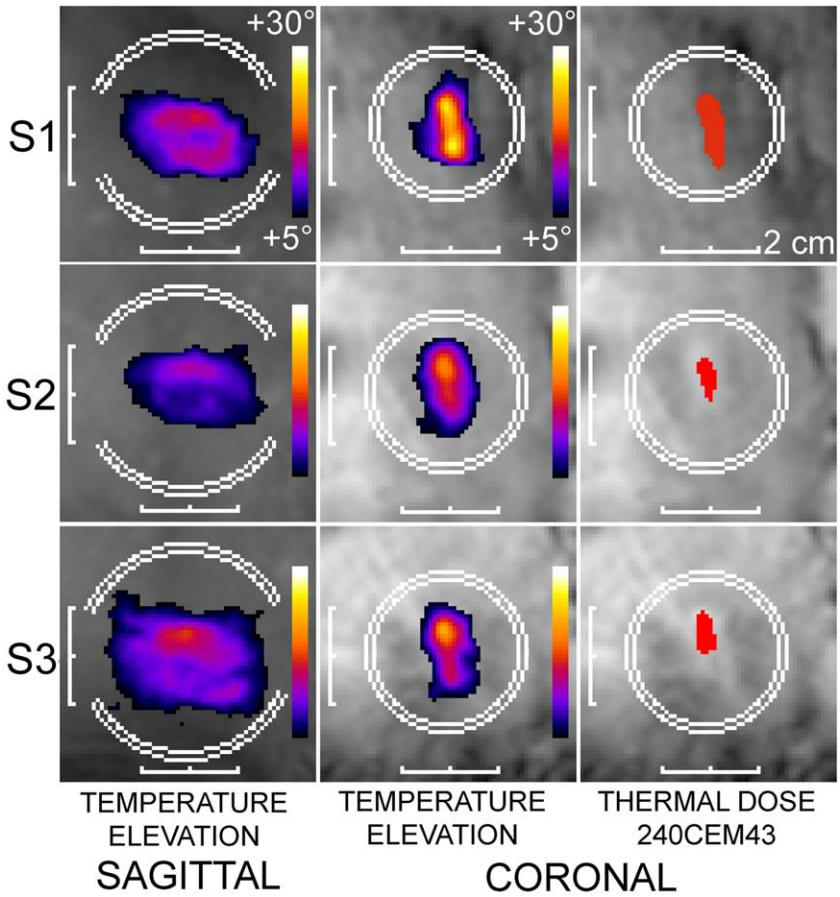

FIG. 5. HIFU-induced temperature elevation and accumulated thermal dose without motion compensation for three individual sonications (150 W, 36 s): S1, S2, and S3. Each row corresponds to a different location in the sample, allowing at least a 20-mm gap between sonications. The circular border (open in the sagittal plane, closed in the coronal plane) for near-harmonic referenceless thermometry is shown in white. Note the embedded scales of distances and temperature elevation color bar.

parameters were 60 W of acoustic power over 64 s for the motion-tracking experiment, and 90 W over 64 s for the fixed focal point experiment. For the first case shown, the mean/minimum/maximum deviation between PRFS and fluoroptic thermometry was –0.5/–2.2/0.6°C, respectively. For the second case, the mean/minimum/maximum deviation was –0.2/–2.2/1.7°C, respectively. These two experiments yielded similar temperature curves at the location of the fluoroptic sensor, despite a ratio of 1.42 in applied energy (an effect of HIFU beam steering and locking-on target). Small periodic oscillations of approximately ±1°C amplitude corresponding to the motion cycle of the ex vivo tissue were noticed on the multibaseline motion-corrected PRFS thermometry. These were caused by an imperfect matching between the position of the fluroptic tip in the actual GRE data and the best-scoring reference frame chosen from the pixel-wise/frame-wise motion atlas. The local field gradient induced by the susceptibility artifact from the air shielding of the fluoroptic tip was therefore not perfectly canceled with the GRE-phase multireference subtraction, when the tissue sample was moving. Overall, these effects were measurable, but the motion-corrected PRFS thermometry matched the "gold standard" data within 1°C.

Motion Compensation in Free-Breathing Volunteers

The tracking factors between landmark displacement on US images and the applied MR slice shift ranged from 0.9 to 1.2. The third tracking factor between chest wall displacement, as seen by the MR navigator and the applied MR slice shift, ranged from 0.7 to 1.0. The SNR of the magnitude images in the liver was calculated using the dual-acquisition subtraction method (32) applied to two successive images under apnea. It ranged from 33 to 56, excluding the pixels belonging to blood vessels. Blood vessels that were orientated perpendicular to the sagittal slice had sufficient conspicuity versus the surrounding parenchyma MR signal in the segmented GRE-EPI magnitude data, to enable accurate registration (see Fig. 8a and Supporting Fig. S1). The vessel signal was typically higher than the neighboring parenchyma voxels by a factor of 2. Motion compensation, as described in this study, suppressed 65 to 80% of the apparent sagittal motion of blood vessels (Fig. 8b and Supporting Fig. S1). Quantitatively, the mean absolute deviation in the coronal GRE-EPI magnitude data for the blood-vessel locations A, B, C, D, E, and F (as indicated by arrows in Fig. 8 and Supporting Fig. S1), measured during 36 s along the HF direction with/without motion compensation, was 1.7/8.7, 2.7/10, 3.4/10.5, 2.2/11.2, 2.0/9.8, 2.4/10.8 mm, and 1.0/2.9, 0.8/2.4, 0.8/2.5, 1/1, 1/1, 1/1.4 mm along the LR direction with/without motion compensation, respectively.

Typically, the described method reduced the motion mean absolute deviation by a factor of 5 at the location for which the scaling factor US/MR was optimized. In our case, this yielded mean absolute deviation values of

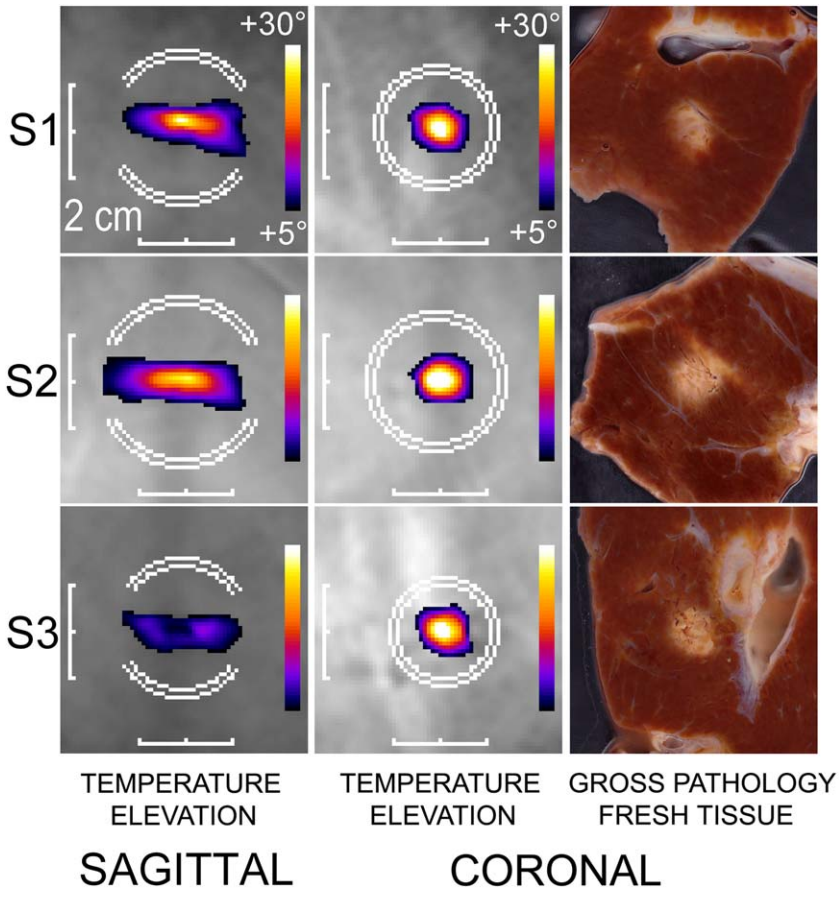

FIG. 6. Three-dimensional motion-compensated sonication with US-MRgHIFU in three individual sonications, S1, S2 and S3 (36 s), performed in a second sample of the same excised liver. Each row corresponds to a different location in the tissue, allowing at least a 20-mm gap between sonications. The applied acoustic power was 150 W at the natural focus and was compensated for lateral steering. Magnetic resonance thermography and gross histology are displayed at the same geometric scale. Graphical properties are the same as for Figure 5.

the principal component HF in the range of 1.7 to 3.4 mm, with the best-site correction mean absolute deviation equal or less than the voxel size.

Analyzing the phase data of the segmented GRE-EPI motion-compensated acquisitions, the nonharmonic term of Laplacian operator ranged between $-1.7 \cdot 10^{-4}$ and $1.55 \cdot 10^{-3}$ rad/mm^2 (mean $\pm$ standard deviation 0.6 ± 0.34 °C rad/mm^2), calculated for a circular ROI of 52-m diameter (Figs. 9a and 9b). The average spatial accuracy of the baseline near-harmonic referenceless PRFS thermometry ranged between –0.50 and 0.52°C (mean $\pm$ standard deviation 0.14 ± 0.34°C). These values showed no correlation to the stages of breathing cycle (i.e., end of exhalation, intermediate inhalation, end of inhalation, intermediate exhalation) and closely matched the values from the original report (22), in which no motion compensation of k-space segments was applied. These results demonstrate an absence of significant distortion of the near-harmonic feature of the GRE-EPI signal at large spatial scale. The spatial average precision of referenceless

Table 1
MRgHIFU Sonication (150 W, 36 s) in Static and Moving Tissue, Without and With Motion Compensation, of the Focal Point in 2D (In-Plane US Imaging) or 3D (In-Plane US Imaging and Orthogonal MR Navigator)

ID	Tissue motion	In-plane peak-to-peak motion amplitude (mm)	Through-plane peak-to-peak motion amplitude (mm)	HIFU focal point steering for motion tracking	Tracking factors (ultrasound HF, ultrasound LR, MR NAV AP)	Maximum temperature elevation (°C)
1	None (static)	0	0	No	(0, 0, 0)	45.0
2	None (static)	0	0	No	(0, 0, 0)	42.8
3	Periodic	8	3	No	(0, 0, 0)	22.2
4	Periodic	8	3	No	(0, 0, 0)	18.4
5	Periodic	8	3	No	(0, 0, 0)	19.4
6	Periodic	8	3	2D	(1.25, 1.25, 0)	38.2
7	Periodic	8	3	2D	(1.25, 1.25, 0)	33.0
8	Periodic	8	3	3D	(1.1, 1.1, 0.4)	40.8
9	Periodic	8	3	3D	(1.1, 1.1, 0.4)	38.5
10	Periodic	8	3	3D	(1.1, 1.1, 0.4)	44.4

Note: Experiments were performed on tissue samples extracted from the same bovine liver. The time period of the tissue motion was 8 s. Applied acoustic power was compensated for lateral steering when motion tracking was used.

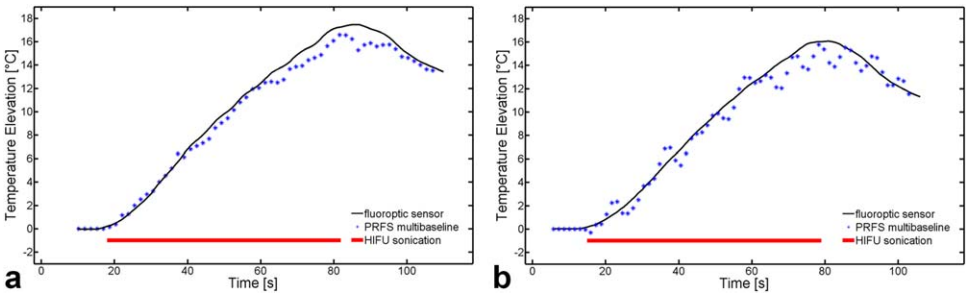

FIG. 7. Comparison of multibaseline PRFS thermometry versus the fluoroptic sensor in moving tissue for MRgHIFU sonications. **a**: Focal point is fixed (90 W, 64 s). **b**: Focal point is tracking the tissue motion using the 3D correction method (60 W, 64 s).

thermometry over the breathing cycle ranged between 0.68 and 1.25°C. It should be noted that a higher spatial resolution, and hence a smaller voxel volume and lower intrinsic SNR, was defined in the present study as 20 to 32 mm^3, as compared with the previous one of 48 mm^3 in (22). This choice was justified by the need for spatial registration of magnitude data features (blood vessels), as described previously. When examining in detail the different stages of the breathing cycle, some structured patterns of apparent nonzero baseline temperature had a slight tendency to be accentuated during the rapid motion stages on the order of additional 10%, as illustrated in Supporting Figure S2. The pixel-wise temporal standard deviation of the baseline referenceless thermometry in the liver of four volunteers as shown in Figures 9c to 9f was better than 1.5°C in 91.3, 100, 72.2, and 89.7% of the pixels, and better than 2°C in 98.6, 100, 96.8, and 100% of the pixels, respectively. Some patient-specific, regional-enhanced uncertainty was observed, which was not correlated with the phase-encoding direction. A more detailed analysis of the liver motion of volunteer 3 showed an anatomical variant with particular tilt patterns in the sagittal plane, which in turn yielded less-effective compensation using the rigid translation approach.

DISCUSSION

The application of HIFU to the abdominal and thoracic region requires motion tracking of the targeted organ and acoustic beam steering. This could be achieved in the present study using a hybrid guiding technique (US-MRgHIFU), involving the complementary and noninvasive imaging modalities of US and MRI.

Our setup used 2D US imaging that is fast, motion-robust, readily available and inexpensive, combined with a one-dimensional MR pencil-beam navigator that required limited additional time in the MR pulse sequence. This combination offered high temporal resolution and precision of the tracking signal. The simultaneous use of three orthogonal pencil-beam navigators may be time-consuming in the MR pulse-sequence chronogram, and furthermore would produce inconvenient signal-void saturation regions on thermometry images. A viable option in this case would be the use of spectrally selective navigators for adipose tissue tracking (33,34).

The principal component of the motion (cranio-caudal, or HF) was monitored and tracked using US, minimizing the out-of-plane motion in the US images. At no additional time penalty, the LR direction was compensated within the same step. Careful adjustment of the US imaging probe position was required to acquire, as close as possible, the principal component of motion in the US imaging plane. The US imaging plane was set slightly oblique per need, parallel to the time-averaged motion vector of the sample, as motion through the US imaging plane may reduce the stability of the optical flow tracking algorithm. Optionally, the motion information along the third dimension, as provided by the MR navigator, could be ignored, but this yielded a 10 to 15% energy loss at focus. The thermal dose being nonlinear, this effect may be significant in vivo. Nevertheless, the third dimension becomes more important when the US imaging plane cannot capture the principal components, such as due to a restricted acoustic window. In this case, the actual motion vector is reconstructed from three linear independent projections after registration of the US imaging plane with the MR coordinates.

The active motion tracking enabled a sonication of nearly 100% duty cycle. Without motion compensation, the acoustic energy is dispersed, creating a risk of thermal damage to the surrounding critical structures in the treated organ, as well as ineffective heating of the focal spot, therefore requiring increased energy to elevate the temperature. The higher delivered energy increases the

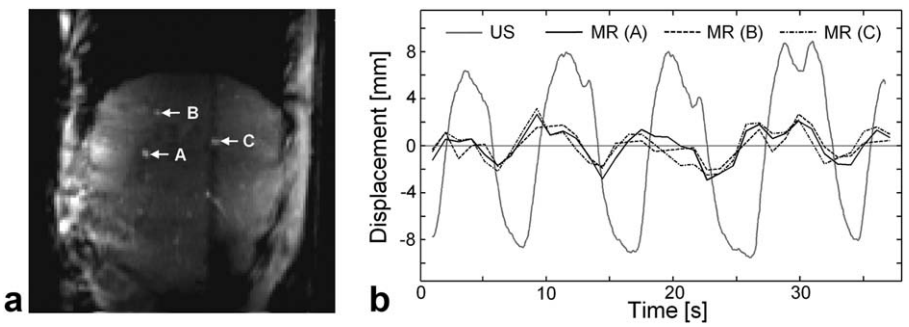

FIG. 8. Motion tracking and compensation in vivo in the liver of volunteer 1. **a**: Magnitude GRE-EPI image in a sagittal plane, illustrating the inflow blood hyperintense signal of three hepatic vessels (A, B, and C). **b**: Kinetic data of the principal motion component (HF direction) extracted simultaneously from the tracked ROI in the US imaging, and, respectively, from the motion-compensated MR signal of the hepatic vessels (A, B, and C).

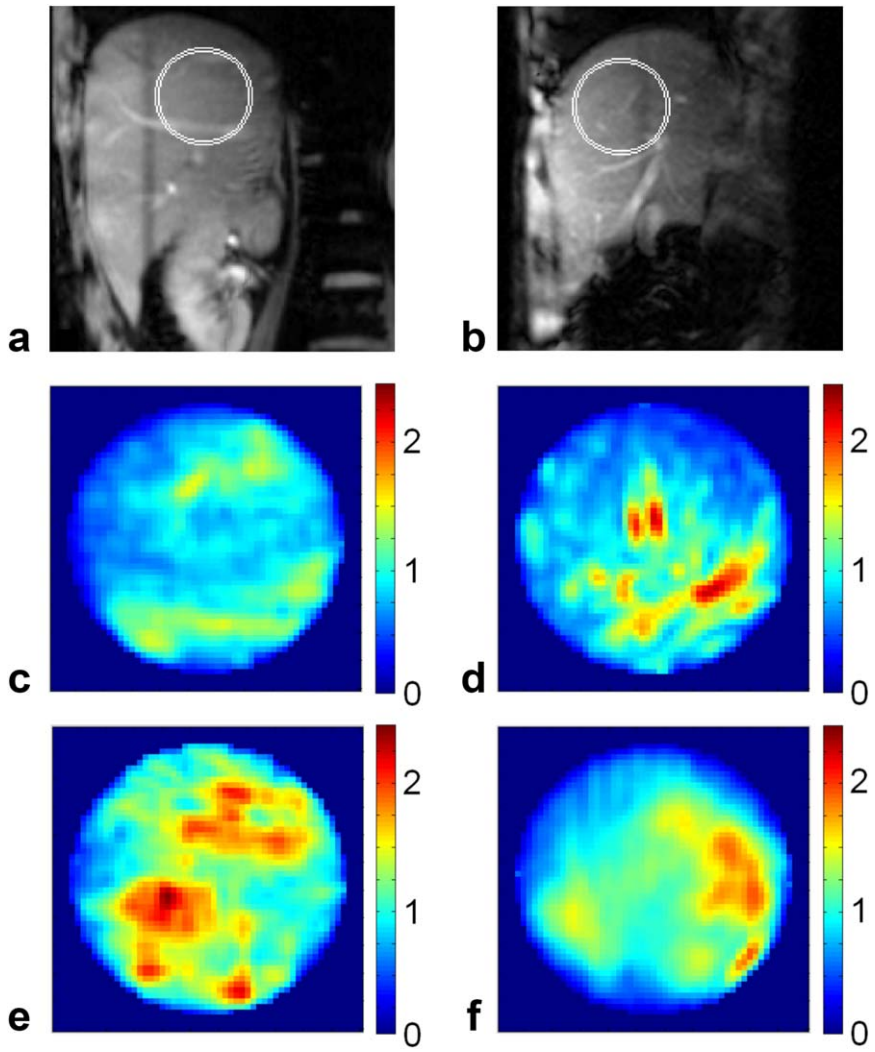

FIG. 9. Near-harmonic referenceless PRFS thermometry applied to motion-compensated GRE-EPI data in liver. **a, b**: Sample coronal magnitude images for volunteers 1 and 2, together with the double-border circular ROI used for the reconstruction of the background phase. **c, f**: Pixel-wise temporal standard deviation of referenceless thermometry (in Celsius) during a 2-min acquisition, provided for the four volunteers successively. The field of view shown is 55-mm square.

risk of side effects. When applied ex vivo, in periodic and nonrigid motion, the method achieved full 3D motion compensation, restoring "static-like" local conditions for sonication in the ROI. Motion compensation clearly enabled a higher temperature elevation to be achieved than a sonication without motion compensation. The thermal dose calculation and the gross pathologies after the experiment both indicated that the acoustic energy was precisely focused on the moving target in all three directions within a mean deviation ± 1 mm, even though the ex vivo tissue was moving and deforming during the sonication. Validation of the segment-based motion-corrected PRFS thermometry versus a gold standard method in the MRgHIFU setup is a rather complex question, as the therapeutic ultrasound may be absorbed directly by the sensor. Here, acoustic shielding of the sensor was effectively achieved at a price of marginal susceptibility artifacts around the tip. Application of focused ultrasound at the sensor tip yielded a sharp thermal build-up, as compared with the amplitude of motion, an essential test condition for our approach.

Beneficially for further application to free-breathing patients, no a priori information about the movement was required. Irregular amplitude of motion observed in healthy volunteers under free-breathing conditions could also be handled, requiring no model-learning stage before treatment because of the use of this real-time method without any background model. In addition to respiratory motion, upper abdomen targets may also be affected by higher motion complexity caused by coughing or cardiac or peristaltic motion.

Liver data acquired in four volunteers using the 3D compensation method demonstrated high SNR and low distortion. The residual motion of the compensated ROI using locally optimized tracking factors was circumscribed inside the thermal diffusion sphere, defined by its specific diameter $2 \cdot \sqrt{2 \cdot D \cdot \Delta t} \approx 6$ mm, in which D is the thermal diffusivity assumed isotropic, typically $0.13\,\mathrm{mm}^2/\mathrm{s}$ (35), and Δt is the elementary sonication duration on the order of 30 s.

The prospective motion compensation of the MR thermometry is also advantageous, as it is then not necessary to register the temperature maps in moving tissue for the referenceless calculation. The ROI, used for referenceless thermometry, appears motionless in the slice coordinate reference frame.

One potential limitation, before starting the intraoperatory acquisition of motion-compensated MR data,

was the necessity to adjust the scaling factors between the US-measured motion vectors and the applied MR slice position compensation. In other words, the motion information was not obtained directly from the treated region. Therefore, we relied on indirect tracking by visualization from US and MR. This becomes a critical question when dealing with nonrigid motion. The in-plane scaling factors (cranio-caudal and LR) typically ranged between 0.6 and 1.25. Nonetheless, in principle, the adjustment of the scaling factors can be achieved automatically by minimizing the residual motion of the ROI in the MR thermometry magnitude data. It should be noted that the translational scaling factor between B-mode tracking in the US imaging plane and the MR local landmark was adjusted in a site-specific manner, whereas the liver motion was nonrigid. Therefore, the apparent motion suppression could only be optimized locally and could not be simultaneously achieved in the entire liver. Deformation and local rotation are considered as a source of residual phase shifts after the subtraction of the referenceless model background, as visible in Figure 9e.

Another limitation of this study was the absence of a true histological reference that was detectable both in pre-operative MRI and in postmortem macroscopic slices (36), as absolute proof of the ballistic accuracy of the motion-compensated US-MRgHIFU during ex vivo ablation studies. Although sharply delineated and static tissue–like lesions were produced with motion-compensated single-focus sonications in moving bulk tissue, the accurate positioning of the focal point on a true target at a predefined location was not addressed in this study. Finally, we did not implement active temperature control at the focus. Therefore, the temperature elevation was not accurately reproducible from one experiment to another, despite similar setup and identical acoustic parameters (36 s/150 W/5.4 kJ). This was primarily due to slight differences in sample geometry (e.g., incidence angle of the HIFU beam on the tissue surface, focal point depth). Nonetheless, the difference of the focal point temperature elevation with and without motion compensation was clearly demonstrated, as the heating improvement largely exceeded the interexperiment data fluctuation.

Further in vivo validation of the method is required, involving additional experimental challenges such blood perfusion in the liver parenchyma and avoiding near- and far-field side effects. Moreover, a tissue marker as a ballistic target is foreseen as proof of absolute spatial accuracy of the method.

CONCLUSIONS

The hybrid US-MRgHIFU 3D method for the treatment of abdominal organs with HIFU guided simultaneously by US and MRI was demonstrated as proof of concept in an ex vivo feasibility study. It enabled motion-compensated ablations, which appear similar to the static-like conditions. The MR thermometry was prospectively motion-compensated at a high frame rate, which provided 1°C precision for temperature map validation versus a gold standard method. Subsequent baseline thermometry was also demonstrated in volunteer acquisitions.

ACKNOWLEDGMENTS

The Center of Biomedical Imaging (CIBM) of Switzerland is acknowledged for access to the MR imaging infrastructure. Real-time data transfer software from the MR host computer was provided by Siemens Healthcare, MR Division, Erlangen (Dr. Jörg Roland, Dr. Patrick Gross). Mrs. Orane Lorton, M.S., is acknowledged for her help in engineering an MR-compatible ultrasound probe and her contributions to the graphical presentation.

REFERENCES

1. Jolesz MM. MRI-guided focused ultrasound surgery. Annu Rev Med 2009;60:417–430.
2. Hindley J, Gedroyc WM, Regan L, et al. MRI guidance of focused ultrasound therapy of uterine fibroids: early results. AJR Am J Roentgenol 2004;183:1713–1719.
3. Huber PE, Jenne JW, Rastert R, Simiantonakis I, Sinn HP, Strittmatter HJ, von Fournier D, Wannenmacher MF, Debus J. A new noninvasive approach in breast cancer therapy using magnetic resonance imaging-guided focused ultrasound surgery. Cancer Res 2001;61:8441–8447.
4. Martin E, Jeanmonod D, Morel A, Zadicario E, Werner B. High-intensity focused ultrasound for noninvasive functional neurosurgery. Ann Neurol 2009;66:858–861.
5. Catane R, Beck A, Inbar Y, et al. MR-guided focused ultrasound surgery (MRgFUS) for the palliation of pain in patients with bone metastases—preliminary clinical experience. Ann Oncol 2007;18:163–167.
6. Sapareto SA, Dewey WC. Thermal dose determination in cancer therapy. Int J Radiat Oncol Biol Phys 1984;10:787–800.
7. Pernot M, Tanter M, Fink M. 3-D real-time motion correction in high-intensity focused ultrasound therapy. Ultrasound Med Biol 2004;30:1239–1249.
8. de Oliveira PL, de Senneville BD, Dragonu I, Moonen CT. Rapid motion correction in MR-guided high-intensity focused ultrasound heating using real-time ultrasound echo information. NMR Biomed 2010;23:1103–1108.
9. Feinberg DA, Giese D, Bongers DA, Ramanna S, Zaitsev M, Markl M, Günther M. Hybrid ultrasound MRI for improved cardiac imaging and real-time respiration control. Magn Reson Med 2010;63:290–296.
10. Arvanitis CD, Livingstone MS, McDannold N. Combined ultrasound and MR imaging to guide focused ultrasound therapies in the brain. Phys Med Biol 2013;58:4749–4761.
11. Marien A, Gill I, Ukimura O, Nacim B, Villers A. Target ablation—image-guided therapy in prostate cancer. Urol Oncol 2014;32:912–923.
12. Rueff LE, Raman SS. Clinical and technical aspects of MR-guided high intensity focused ultrasound for treatment of symptomatic uterine fibroids. Semin Intervent Radiol 2013;30:347–353.
13. de Senneville BD, Ries M, Maclair G, Moonen C. MR-guided thermotherapy of abdominal organs using a robust PCA-based motion descriptor. IEEE Trans Med Imaging 2011;30:1987–1995.
14. Ries M, de Senneville BD, Roujol S, Berber Y, Quesson B, Moonen C. Real-time 3D target tracking in MRI guided focused ultrasound ablations in moving tissues. Magn Reson Med 2010;64:1704–1712.
15. Holbrook AB, Ghanouni P, Santos JM, Dumoulin C, Medan Y, Pauly KB. Respiration based steering for high intensity focused ultrasound liver ablation. Magn Reson Med 2014;71:797–806.
16. Celicanin Z, Auboiroux V, Bieri O, Petrusca L, Santini F, Viallon M, Scheffler K, Salomir R. Real-time method for motion-compensated MR thermometry and MRgHIFU treatment in abdominal organs. Magn Reson Med 2014;72:1087–1095.
17. Auboiroux V, Petrusca L, Viallon M, Goget T, Becker CD, Salomir R. Ultrasonography-based 2D motion-compensated HIFU sonication integrated with reference-free MR temperature monitoring: a feasibility study ex vivo. Phys Med Biol 2012;57:N159–N171.
18. Ries M, de Senneville BD, Regard Y, Moonen C. Combined magnetic resonance imaging and ultrasound echography guidance for motion compensated HIFU interventions. In Proceedings of the 20th Annual Meeting of ISMRM, Melbourne, Australia, 2012. p. 1575.

19. Auboiroux V, Petrusca L, Viallon M, Muller A, Terraz S, Breguet R, Montet X, Becker CD, Salomir R. Respiratory-gated MRgHIFU in upper abdomen using an MR-compatible in-bore digital camera. BioMed Res Int 2014;2014:421726.
20. Rieke V, Pauly KB. MR thermometry. J Magn Reson Imaging 2008;27: 376–390.
21. Rieke V, Vigen KK, Sommer G, Daniel BL, Pauly JM, Butts K. Referenceless PRF shift thermometry. Magn Reson Med 2004;51:1223–1231.
22. Salomir R, Viallon M, Kickhefel A, et al. Reference-free PRFS MR-thermometry using near-harmonic 2-D reconstruction of the background phase. IEEE Trans Med Imaging 2012;31:287–301.
23. de Senneville BD, Roujol S, Moonen C, Ries M. Motion Correction in MR thermometry of abdominal organs: a comparison of the referenceless vs. the multibaseline approach. Magn Reson Med 2010;64:1373–1381.
24. Rieke V, Kinsey AM, Ross AB, Nau WH, Diederich CJ, Sommer G, Pauly KB. Referenceless MR thermometry for monitoring thermal ablation in the prostate. IEEE Trans Med Imaging 2007;26:813–821.
25. Hardy CJ, Pearlman JD, Moore JR, Roemer PB, Cline HE. Rapid NMR cardiography with a half-echo M-mode method. J Comput Assist Tomogr 1991;15:868–874.
26. Nehrke K, Börnert P, Groen J, Smink J, Böck JC. On the performance and accuracy of 2D navigator pulses. Magn Reson Imaging 1999;17: 1173–1181.
27. Petrusca L, Cattin P, de Luca V, et al. Hybrid ultrasound/magnetic resonance simultaneous acquisition and image fusion for motion monitoring in the upper abdomen. Invest Radiol 2013;48:333–340.
28. Shi J, Tomasi C. Good features to track. In Proceedings of the IEEE Computer Society Conference on Computer Vision and Pattern Recognition, Seattle, Washington, USA, 1994. pp. 593–600.
29. Lucas B, Kanade T. An iterative image registration technique with an application in stereo vision. In Proceedings of the 7th International Joint Conference on Artificial Intelligence, Vancouver, British Columbia, Canada, 1981. pp. 674–679.
30. von Bouguet JY. Pyramidal implementation of the Lucas-Kanade feature tracker. OpenCV Documentation, Intel Corp, Microprocessor Research Labs, Technical Report (1999).
31. Vigen KK, Daniel BL, Pauly JM, Butts K. Triggered, navigated, multi-baseline method for proton resonance frequency temperature mapping with respiratory motion. Magn Reson Med 2003;50:1003–1010.
32. Kickhefel A, Rosenberg C, Roland J, Viallon M, Gross P, Schick F, Hosten N, Salomir R. A pilot study for clinical feasibility of the near-harmonic 2D referenceless PRFS thermometry in liver under free breathing using MR-guided LITT ablation data. Int J Hyperthermia 2012;28:250–266.
33. Köhler MO, de Senneville BD, Quesson B, Moonen CT, Ries M. Spectrally selective pencil-beam navigator for motion compensation of MR-guided high-intensity focused ultrasound therapy of abdominal organs. Magn Reson Med 2011;66:102–111.
34. Celicanin Z, Bieri O, Scheffler K, Santini F. Spectrally selective crossed-pair navigator. In Proceedings of the 20th Annual Meeting of ISMRM, Melbourne, Australia, 2012. p. 3408.
35. Duck FA. Physical properties of tissue: a comprehensive reference book. London: Academic Press; 1990. p. 16.
36. Petrusca L, Viallon M, Breguet R, et al. An experimental model to investigate the targeting accuracy of MR-guided focused ultrasound ablation in liver. J Transl Med 2014;12:12.

SUPPORTING INFORMATION

Additional Supporting Information may be found in the online version of this article.

Fig. S1. Motion tracking and compensation in vivo in the liver for volunteer 2. **a**: Magnitude GRE-EPI image in a sagittal plane, illustrating the inflow blood hyperintense signal of three hepatic vessels (D, E, and F). **b**: Kinetic data of in-plane motion (HF and AP directions, respectively) extracted from noncompensated MR signal of the hepatic vessels (D, E, and F). **c**: Kinetic data of in-plane motion (HF and AP directions, respectively) extracted from motion-compensated MR signal of the same vessels.

Fig. S2. Residual phase shifts after the subtraction of the referenceless model background using motion-compensated data acquired in the coronal plane, converted to the equivalent temperature (○C) for the volunteer 1, provided at four different stages of one breathing cycle: inspiration (**a**), lung maximum inflation (**b**), expiration (**c**), and lung minimum inflation (**d**). The field of view shown is 55-mm square.